

### Available online at www.sciencedirect.com





journal homepage: www.elsevier.com/locate/jmrt

## **Original Article**

# Mechanical behavior and shear band of a powdermetallurgy-fabricated CoCrFeMnNi high-entropy alloy during high strain-rate deformation



Wenshu Li  $^b$ , Bingfeng Wang  $^{a,b,*}$ , Xiaoxia Huang  $^b$ , Bin Liu  $^a$ , Jamieson Brechtl  $^c$ , Peter K. Liaw  $^{d,**}$ 

- <sup>a</sup> State Key Laboratory of Powder Metallurgy, Central South University, Changsha, 410083, PR China
- <sup>b</sup> School of Materials Science and Engineering, Central South University, Changsha, 410083, PR China
- <sup>c</sup> The Bredesen Center for Interdisciplinary Research and Education, The University of Tennessee, Knoxville, TN, 37996, USA
- <sup>d</sup> Department of Materials Science and Engineering, The University of Tennessee, Knoxville, TN, 37996, USA

### ARTICLE INFO

Article history: Received 18 May 2022 Accepted 27 September 2022 Available online 5 October 2022

Keywords:

High-entropy alloy Powder metallurgy Mechanical property Serration behavior Shear localization

### ABSTRACT

High-entropy alloys (HEAs) fabricated by powder metallurgy are considered to exhibit extremely-great potential application values in the field for high-speed impact deformation due to their uniform microstructures and compositions. The mechanical behavior of a powder-metallurgy-fabricated (PM) CoCrFeMnNi HEA was investigated at room temperature with strain rates ranging from 1200 s<sup>-1</sup> to 2800 s<sup>-1</sup>. It was found that the serration behavior and shear localization of the alloy under dynamic conditions occurred. Results also indicated that the serrated flow took place in the PM CoCrFeMnNi HEA during mechanical deformation at high strain rates (>1000 s<sup>-1</sup>) and became more pronounced as the strain rate increased. Furthermore, it was determined that the yield-strength values of the PM CoCrFeMnNi HEA were sensitive to strain rates, where the values increased from 500 MPa to 700 MPa when the strain rates increased from  $1200 \text{ s}^{-1}$  to  $2800 \text{ s}^{-1}$ . Shear bands with a width of about 20 µm were generated in the PM CoCrFeMnNi HEA after the shear stress reached a maximum value of 635 MPa, which corresponded to a nominal strain of about 8.71. Nanotwins and ultrafine-equiaxed grains with a diameter of about 150 nm also developed at the core of the shear band during deformation. The results revealed that the strength of the shear band was much higher than that of the matrix grain. Nanotwins in the shear band were composed of a single face-centered-cubic (FCC) structure with the twin plane of  $(\overline{111})$ , which could be formed via a rotational dynamic recrystallization (RDR). © 2022 The Authors. Published by Elsevier B.V. This is an open access article under the CC BY-NC-ND license (http://creativecommons.org/licenses/by-nc-nd/4.0/).

<sup>\*</sup> Corresponding author.

<sup>\*\*</sup> Corresponding author.

## 1. Introduction

The equiatomic CoCrFeMnNi high-entropy alloy (HEA), which is also called the Cantor alloy, consists of a single-phase face-centered-cubic (FCC) solid solution that is one of the extensively-investigated HEAs [1–7]. The strength of the CoCrFeMnNi HEA is relatively low (~200 MPa) in the as-cast state [8]. Powder metallurgy is a promising way to prepare the high-strength CoCrFeMnNi HEA with homogeneous compositions and microstructures [9–12]. Materials are required to exhibit excellent mechanical properties and structural stability under high-speed deformation applications, such as impact, collision and penetration in use in the field for tank armors, high-speed trains, and aircraft [13–15].

Serration behavior is characterized by fluctuations in the stress vs. strain curve, and usually occurs in many structural materials when deformed during low-temperature or low strain-rate deformation [16,17]. Zhang et al. [18] noted that in a Zr<sub>64.13</sub>Cu<sub>15.75</sub>Ni<sub>10.12</sub>Al<sub>10</sub> bulk metallic glass (BMG), the magnitude of serrations increased with strain rates ranging from  $10^{-2} \, \text{s}^{-1}$  to  $5 \times 10^{-5} \, \text{s}^{-1}$ . Oh et al. [19] found that in a Fe–18Mn-0.55C steel, serrations occurred under low strain-rate deformation ( $<0.01 \,\mathrm{s}^{-1}$ ) at a temperature of 253 K. Tirunilai et al. [20] reported the serrated flow in a CoCrFeMnNi HEA at a temperature of 35 K and a strain rate of  $3 \times 10^{-4}$  s<sup>-1</sup>. Furthermore, the same HEA could also exhibit serration behavior under high strain-rate deformation (>1000  $s^{-1}$ ) at ambient temperature. Liu et al. and Yao et al. [21,22] studied the serration behavior of the as-cast and forging CoCrFeMnNi HEA, and found that the serration fluctuations became more pronounced with an increase in the strain rate (>1200 s<sup>-1</sup>). The microstructure and composition of the powder-metallurgy-fabricated (PM) CoCr-FeMnNi HEA is more homogeneous than that of the as-cast and forging CoCrFeMnNi HEA, leading to the difference of mechanical behavior in the PM Cantor HEA. So it is necessary to study the serration behavior of the PM CoCrFeMnNi HEA. Such serration behavior illustrates the unstable mechanical behavior of the Cantor alloy during mechanical testing [2,18]. The results also showed that under the high-speed impact, serrations became more prominent in the Cantor alloy as the strain rate increased. The authors concluded that factors, such as high-density dislocation entanglement, large amounts of deformation bands or shear bands, were likely responsible for the exhibited behavior [21].

At present, the refined composite multiscale entropy (RCMSE) [23] and mean field theory (MFT) [24] techniques have been used to analyze the serration behavior of metallic materials. Zhang et al. [25] employed the RCMSE method to analyze the serration behavior in the 5083 medium-entropy aluminum alloy. The results of the analysis revealed that the complexity of the serrated flow increased with an increasing solute concentration, grain size, and plasticity. This increasing complexity was attributed to a greater concentration of solutes available to pin mobile dislocations, leading to a wider variety of interactions that are indicative of more complicated dynamical behavior. Antonaglia et al. [26] employed the MFT method to analyze the serration behavior of the Zr<sub>64.13</sub>Cu<sub>15.75</sub>Ni<sub>10.12</sub>Al<sub>10</sub> BMG at room temperature and strain rates of 1  $\times$  10<sup>-3</sup>, 2  $\times$  10<sup>-4</sup>, and 5  $\times$  10<sup>-5</sup> s<sup>-1</sup>. The results

of the complementary cumulative distribution function (CCDF) analysis showed that the stress-drop magnitude depends on the strain rate and stress. Furthermore, they were able to collapse the CCDF curves, using tuning parameters that are based on the MFT.

Adiabatic shear localization, which is a typical deformation mode under a high strain rate, usually results in softening or even failure of the material. Meyers et al. [27,28] found that the Alo 3CoCrFeNi HEA exhibited remarkable resistance to adiabatic shear localization due to its excellent stain-hardening ability. Yang et al. [29] investigated the effects of microstructure and strain rate on the adiabatic shear sensitivity of a FeMnCoCr HEA. The results indicated that the adiabatic shear sensitivity increased with an increase in the strain rate. Moreover, the smaller grain size was also found to exhibit a lower adiabatic shear sensitivity. In our previous work [30,31], it was determined that the formation of the adiabatic shear band in the CoCrFeMnNi HEA required a very large shear strain, and nanotwins were observed in the shear band. However, the exact nature of the nanotwins was not fully resolved. Therefore, the microstructure and formation mechanism of nanotwins in the shear band needs further study.

In the present work, the high strain-rate mechanical properties of an equiatomic CoCrFeMnNi HEA that was prepared by powder metallurgy are investigated. The serration behavior and the shear localization of the PM CoCrFeMnNi HEA are reported. Furthermore, the microstructures and mechanical properties of the shear band in the PM CoCrFeMnNi HEA are studied. Lastly, the formation mechanism of nanotwins in the shear band is also discussed.

## 2. Materials and methods

## 2.1. Preparation of the CoCrFeMnNi high-entropy alloy

High-purity (99.9 weight percent, wt.%) Co, Cr, Fe, Mn, and Ni powders of an equiatomic ratio were melted in an induction-heated vacuum furnace, and then filled in the atomization chamber, cooled down, and solidified to powders with sizes less than 20 microns. The gas-atomized CoCrFeMnNi HEA powder was put into a graphite die with a diameter of 40 mm. Spark plasma sintering (SPS) was conducted in a HP D 25/3 SPS equipment with a vacuum pressure of 0.001 Pa. The details of the process were described in our previous work [12]. The chemical composition of the PM CoCrFeMnNi HEA is shown in Table 1.

## 2.2. Mechanical-property tests

Cylindrical compressive specimens with a diameter of 6 mm were machined from the HEA samples by an electric discharge

Table 1 — Ch HEA [atomic		•	n of the P	M CoCrFe	MnNi
Flomonto	Fo	Co	Ni	Cr	Mn

Elements	Fe	Co	Ni	Cr	Mn
Composition	20.6	19.80	20.32	19.94	19.34

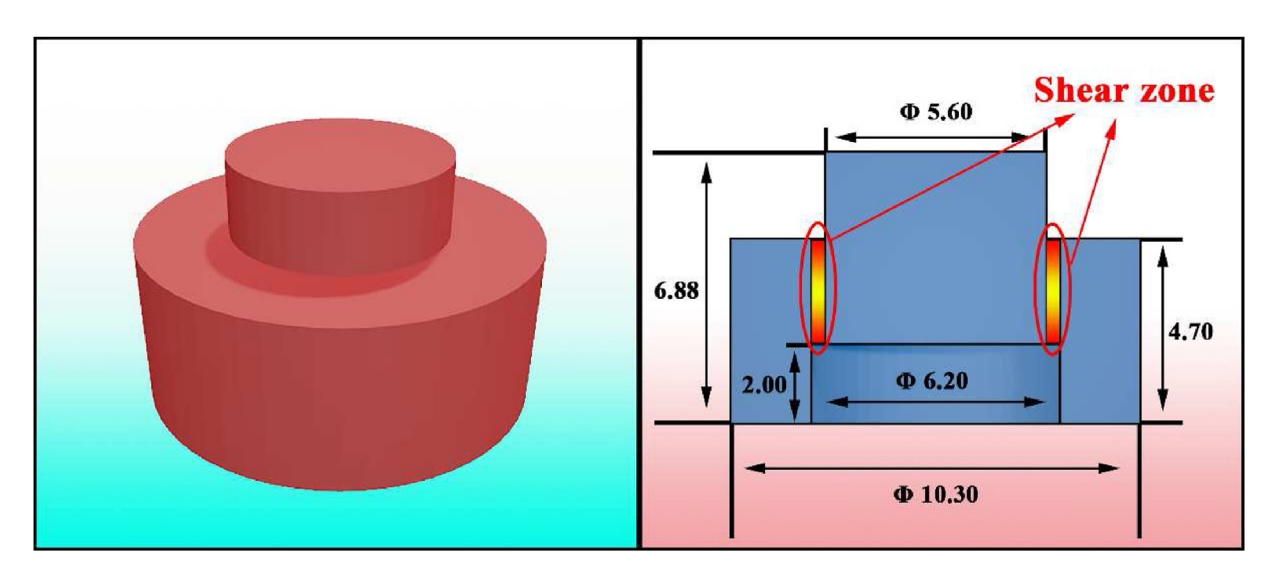


Fig. 1 - Schematic diagrams of the hat-shaped specimen. (dimension in mm).

machine (EDM). Dynamic-compressive tests were performed at the ambient temperature (298 K), using strain rates of approximately 1200 s<sup>-1</sup>, 1260 s<sup>-1</sup>, 2710 s<sup>-1</sup>, and 2800 s<sup>-1</sup> (labelled A, B, C, and D, respectively) by the split-Hopkinson pressure bar. The loading direction was parallel to the cylindrical axis of these specimens. To ensure the uniaxialcompressive condition, the end face of the compressive specimen was ground on each side with the SiC paper and then lubricated. During the process of the impact loading and electrical-signal collection, the advanced waving plastic and anti-jamming technology was adopted [32]. The effect of signal noise on the mechanical behavior is slight according to a large number of comparative tests in our previous work. The shear stress, shear strain, strain rate, true stress, and true strain were calculated from the reflected and transmitted pulses [33]. Full details of the calculation process are given in Appendix A.

High strain-rate experiments employing the split Hopkinson pressure bar with hat-shaped specimens were also performed. The hat-shaped specimen was first adopted by Meyer and Hartmann [32]. Fig. 1 shows the schematic diagram of the hat-shaped specimen. The narrow shear region was designed to produce a shear band due to the shear-strain concentration. The thickness of the designed shear region in the hat-shaped

specimen is about 0.3 mm. The shear stress, shear strain, strain rate, true stress, and true strain of the specimens were obtained from strain gauges [32,34,35]. Full details of the calculation process are given in Appendix A.

## 2.3. Microstructure characterization and nanoindentation

For further characterization, samples were cut from the hatshaped specimen by EDM. The etchant used for the PM CoCr-FeMnNi HEA consisted of the 25 ml ethanol +25 ml hydrochloric acid +5 g copper sulfate pentahydrate. Optical microscopy was carried out, using a DM2500M (Leica, Germany), and further microstructural observations were performed, employing an FEI Quanta-200 scanning electron microscope (SEM) (FEI, Netherlands) operated at 20 kV. The shear band was examined in a Philips XL30 SEM (PHILIPS, Netherlands). The transmission electron microscope (TEM) samples (see Fig. 2) in the shear-band region were fabricated, employing a Helios Nanolab 600i focused ion-beam (FIB) instrument (FEI, USA) with a thinning step of 30 kV Ga<sup>+</sup> ions at a glancing angle of about 2.2° to minimize the irradiation damage to samples. The FIB samples were then characterized by TEM, using the Tecnai G<sup>2</sup> 20 transmission electron microscope

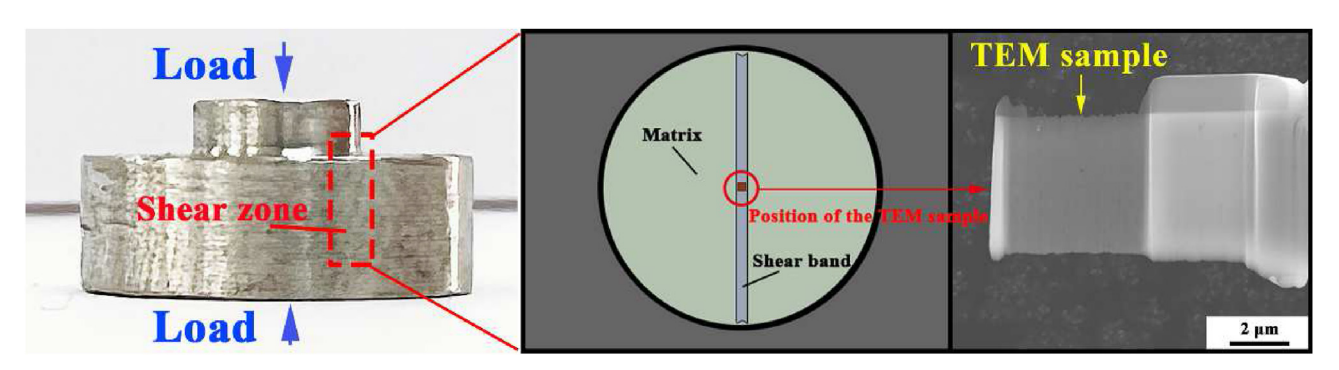
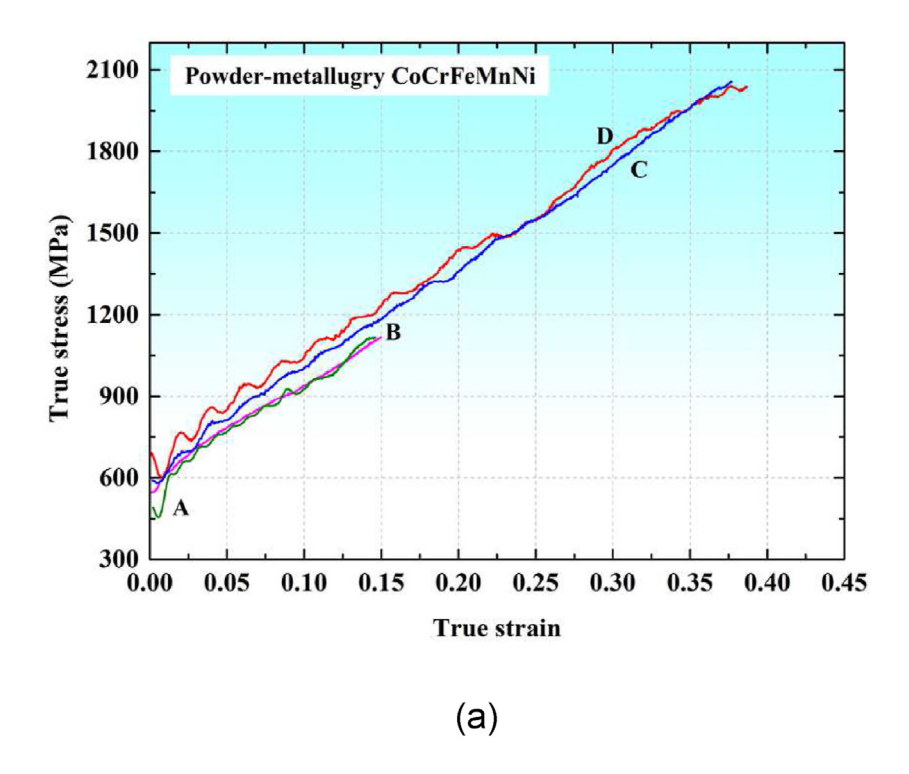


Fig. 2 — Position of the TEM sample in the shear-band region and corresponding image of the TEM lift-out sample, as observed in the SEM.

(FEI, Netherlands) operated at 200 kV, and Tecnai  $G^2$  60–300 polar TEM (FEI, Netherlands) operated at 300 kV. The micrographs of the TEM sample were analyzed employing an Imagepro plus (IPP) image analysis software [36] to characterize the microstructure and grain size in the shear band.

For the purpose of investigating the mechanical properties of the ultrafine-grained structure in the shear band, nano-indentation tests were conducted. Room-temperature nano-indentation testing was carried out in the shear-band region as well as the matrix, using an MCT + UNHT indentation



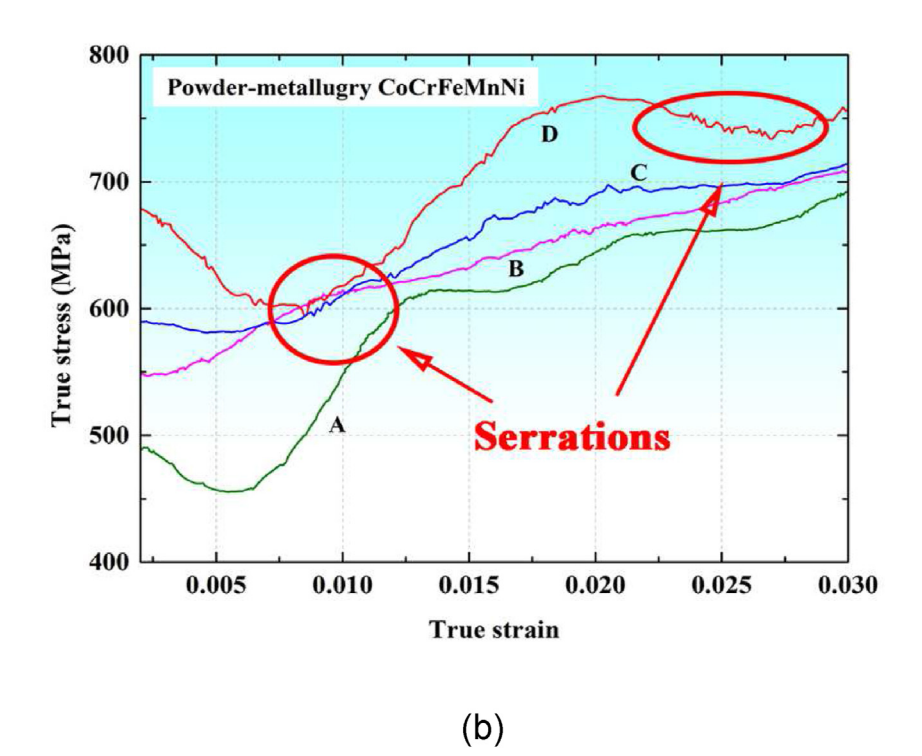


Fig. 3 – Dynamic mechanical response of the PM CoCrFeMnNi HEA deformed at high strain rates ranging from 1200 s<sup>-1</sup> to 2800 s<sup>-1</sup> and ambient temperature. (a) True-strain vs. true-stress curves for the PM CoCrFeMnNi HEA at high strain rates and ambient temperature. (b) Partially-magnified image of (a) which features the serrations.

(CSM, Switzerland) tester equipped with a diamond Berkovich indenter [37]. Here, a maximum load of 20 mN and loading rates of  $0.1 \,\mathrm{s}^{-1}$ ,  $0.2 \,\mathrm{s}^{-1}$ , and  $1 \,\mathrm{s}^{-1}$  were used. Nanoindentations were conducted along the horizontal direction with a spacing of 50 microns. The strength of the shear band and matrix is calculated from the average strength of several different indentations. The strain rates can be expressed as follows [35]:

$$\varepsilon = \dot{\mathbf{h}}/\mathbf{h} = \dot{\mathbf{p}}/2\mathbf{p} \tag{1}$$

where h represents the instantaneous displacement for the Berkovich indenter,  $\dot{h}$  denotes the displacement rate, p is the contact pressure, and  $\dot{p}$  is defined as the loading rate. Hence, the calculated strain rates were  $0.05 \text{ s}^{-1}$ ,  $0.1 \text{ s}^{-1}$ , and  $0.5 \text{ s}^{-1}$ .

#### 2.4. Refined composite multiscale entropy and mean field theory analysis

In the present work, the RCMSE analysis was employed to gain a more fundamental understanding of the complexity of the

the serration statistics of the HEA. More specifically, the CCDF resulting from the analysis was employed to determine the probability of observing a stress-drop that is greater in magnitude than S, which is the stress-drop avalanches [25]. Full details of the derivations are given in Appendix C.

serration dynamics in the presently-studied HEA [38]. Full

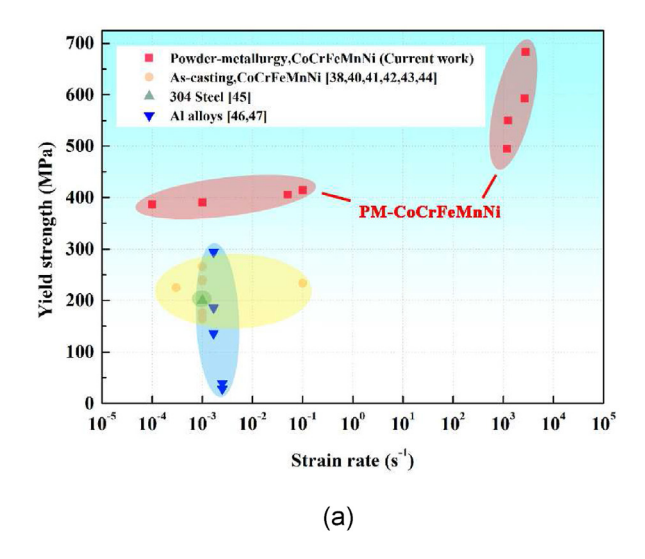
details of the RCMSE technique are given in Appendix B. The

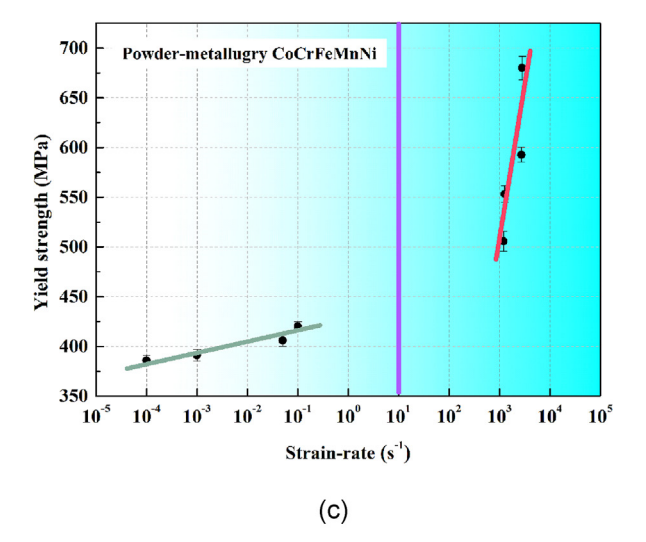
MFT technique was utilized to examine the scaling behavior of

#### Results 3.

#### 3.1. Dynamic-mechanical properties

Fig. 3(a) shows the true-stress vs. true-strain curves of the PM CoCrFeMnNi HEA deformed at high strain rates of 1200–2800 s<sup>-1</sup> at ambient temperature. Fig. 3(b) features the partially-magnified image of Fig. 3(a), which shows that all four samples exhibited the serrated flow under dynamic





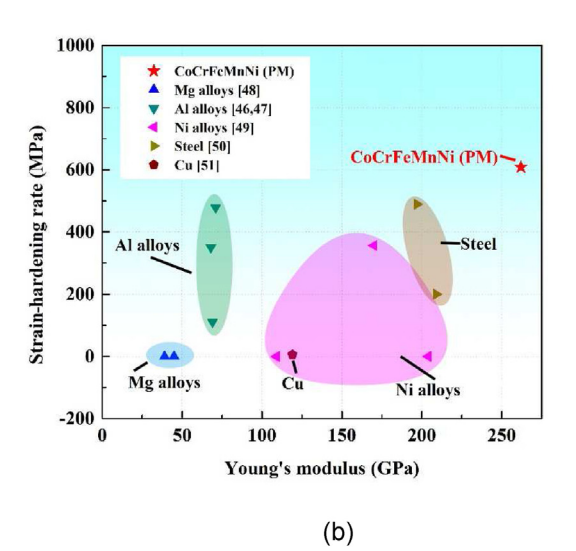
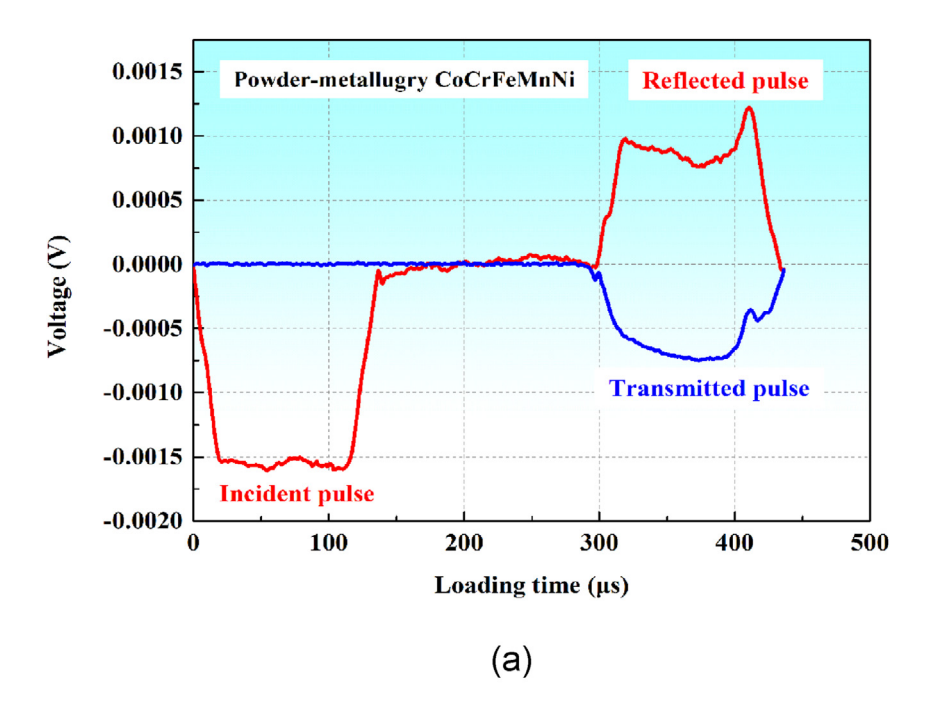


Fig. 4 – Mechanical properties of the PM CoCrFeMnNi HEA. (a) The yield strength vs. strain rate [38,40–47]. (b) The strainhardening rate vs. Young's modulus [46-51]. (c) Semi-log plot of the yield strength vs. the strain-rate-value curves of the PM CoCrFeMnNi HEA.

conditions. Recent studies [2,39,40] have also reported serrations in the same HEA that is currently being investigated. The CoCrFeMnNi HEA prepared by the powder metallurgy displays serrations when deformed at high strain rates (>1000 s $^{-1}$ ), and the serration behavior becomes more pronounced with an increasing strain rate. It is worth mentioning that as compared with the as-cast and deformed alloys, the CoCrFeMnNi HEA prepared by powder metallurgy exhibits smaller serrations when deformed at high strain rates.

The mechanical properties of various materials, including the PM CoCrFeMnNi HEA, as-cast CoCrFeMnNi HEA [39,41–45], 304 stainless steels [46], aluminum alloy [47,48], magnesium alloy [49], nickel-based alloy [50], 316 L steel [51], and copper alloy [52], are compared in Fig. 4(a)–(c). The yield strength of the PM CoCrFeMnNi HEA at low strain rates are adopted from our previous work [12]. It can be seen from Fig. 4(a) that the yield-strength values for the PM CoCrFeMnNi HEA deformed at high strain rates of 1200 s $^{-1}$  - 2800 s $^{-1}$  varies from about



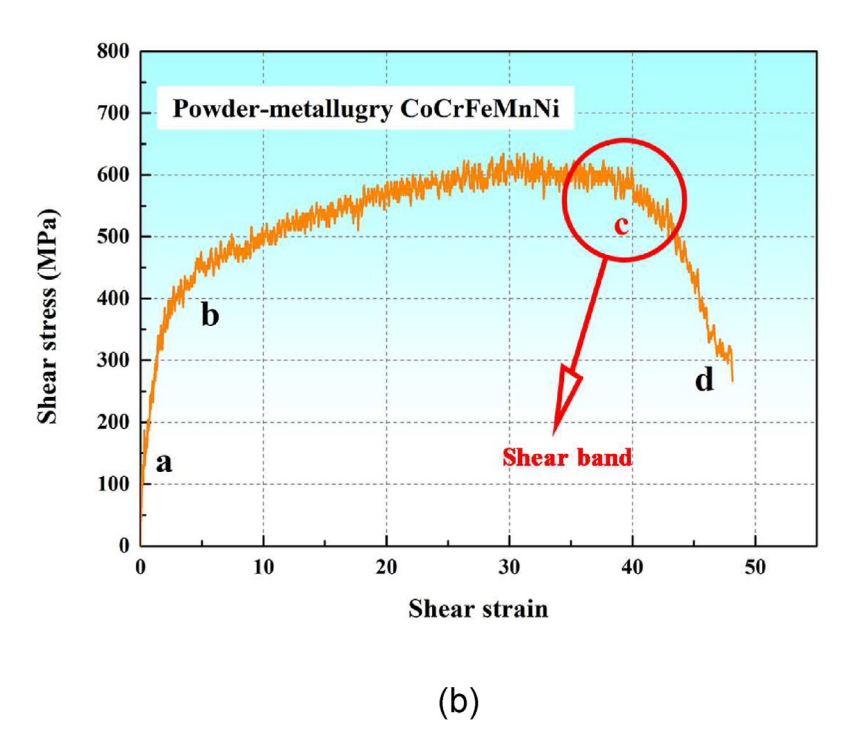


Fig. 5 — Mechanical response of the hat-shaped specimen. (a) Electronic response of the hat-shaped specimen. (b) Shear-stress vs. shear-strain curve of the hat-shaped specimen.

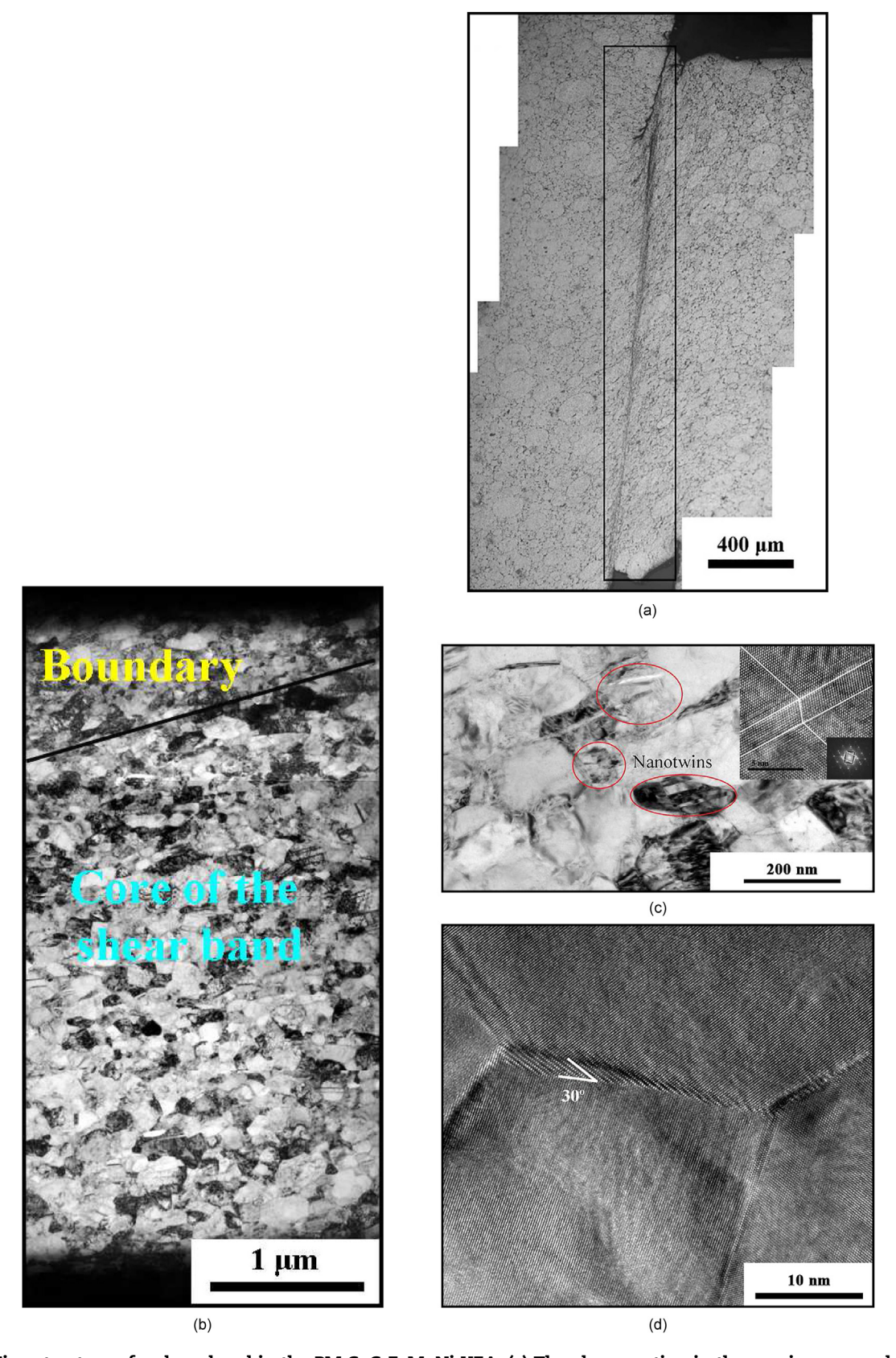


Fig. 6 — Microstructure of a shear band in the PM CoCrFeMnNi HEA. (a) The shear section in the specimen revealed by the optical micrograph. (b) Montage of the bright-field micrographs across the shear band. (c) The microstructure in the core of the shear band. (d) The high-resolution TEM image of the ultrafine-equiaxed grains.

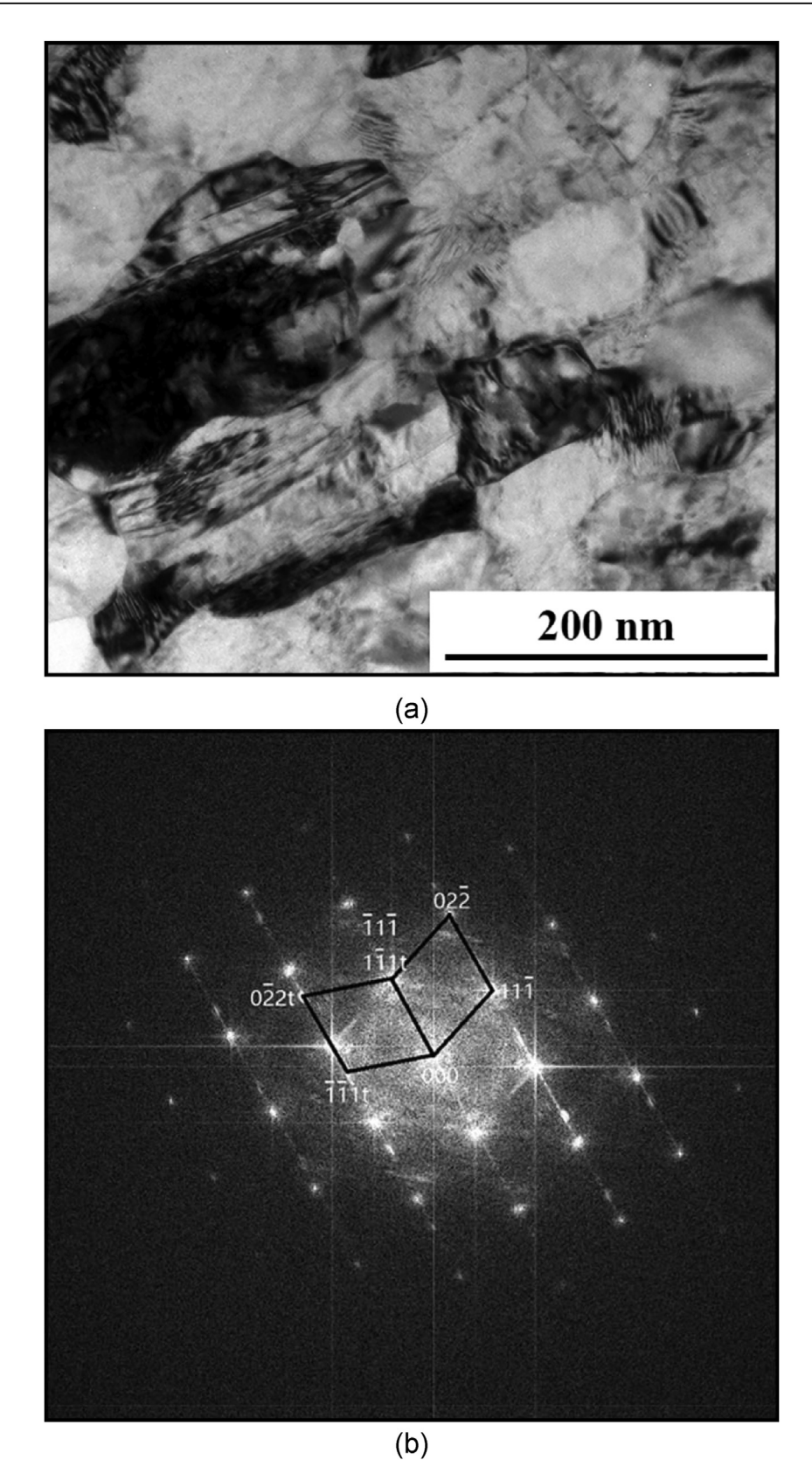


Fig. 7 — Microstructures of nanotwins in the shear band of the PM CoCrFeMnNi HEA. (a) Bright-field image. (b) The Fast Fourier Transform patterns of nanotwins.

500 MPa to 700 MPa. These yield-strength values are generally higher than those associated with low strain rates. Furthermore, the yield strengths of the PM CoCrFeMnNi HEA deformed at different strain rates are greater than those of the as-cast CoCrFeMnNi HEA and other structural materials, as demonstrated in Fig. 4(a). The PM CoCrFeMnNi HEA has the great strain-hardening rate, as compared to the conventional structural metals, as shown in Fig. 4(b). On the one hand, the strain-hardening rate in single phase HEAs are affected by lattice distortion and the degree of atomic size mismatch between constituent elements directly influences lattice distortion. Comparing with the one dominant element alloys, CoCrFeMnNi Cantor alloy exhibits severe lattice distortion, which leads to the great strain hardening rate [4,30]. On the other hand, the PM CoCrFeMnNi HEA, a single-phase facecentered-cubic alloy, has a uniform composition and structure with a fine-grain size of about 600 nm which leads to the high strain hardening capacity in the PM CoCrFeMnNi HEA [12].

Fig. 4(c) presents the yield-strength vs. strain-rate curves of the PM CoCrFeMnNi HEA at ambient temperature. The strainrate sensitivity is defined as follows [53]:

$$m = d(\log \sigma) / d(\log \dot{\varepsilon}) \tag{2}$$

The slope of the line fitting for the data obtained at low strain rates are much less than those obtained at high strain rates. Note that the yield strengths at high strain rates range from about 370 MPa to 700 MPa. Therefore, the yield strengths of the CoCrFeMnNi HEA increase significantly with increasing strain rates (> $10^3$  s<sup>-1</sup>).

## 3.2. Microstructure and nanoindentation of the shear band

The electronic—response curves for the hat-shaped specimen obtained from the split-Hopkinson pressure bar experiment are presented in Fig. 5(a). According to Appendix A, we can calculate the values of shear-stress, shear-strain, and strain-rate, using the data from Fig. 4(a). The forced shearing deformation starts from the first peak value of the strain rate to the last loading stress peak. The entire deformation process lasts approximately 135  $\mu$ s? The average strain rate was determined to be ~410,000 s<sup>-1</sup>. The shear-stress vs. shear-strain curve of the PM CoCrFeMnNi HEA, which exhibits deformation during the shear localization, can be divided into three stages, as shown in Fig. 5(b). In the first stage (a - b), the shear-

stress increases with respect to the true strain due to the shear strain and the strain-rate hardening. In the second stage (b - c), thermal softening becomes the dominant mechanism, and the shear stress increases slower than that of the first stage.

Consequently, the shear-stress for the specimen reaches the maximum value of about 635 MPa where the nominal strain is about 8.71. In the last stage (c - d), the shear-stress sharply decreases with increasing the shear strain, and the thermosviscoplastic instability commences at point c. Therefore, the occurrence of the shear localization in the PM CoCrFeMnNi HEA requires the severe shear deformation. The shear band is generated in the PM CoCrFeMnNi HEA when the value of the shear strain reaches ~30. Therefore, the powder-metallurgy method is promising for fabricating the HEA with high strength and great resistance to the shear localization. It is worth mentioning that the visible serration behavior was also observed in the hat-shaped specimens, which indicates that the higher strain rates could lead to pronounced serrations.

Fig. 6(a) displays an adiabatic shear band in the PM CoCr-FeMnNi HEA. It can be seen that the shear band is a long and straight band located in the designated shear zone. Furthermore, the width of the shear band is about 20  $\mu$ m, which is distinguished from the matrix by continuous boundaries. Fig. 6(b) is a montage of the shear band of the PM CoCrFeMnNi HEA. While the grains in the boundary region are highly elongated along the shear direction, the grain in the core of the shear band tends to be equiaxed. The dimensions of the elongated cell structures in the boundary region are approximately 0.1  $\mu$ m  $\times$  0.7  $\mu$ m. A TEM image of the core of the shear band is shown in Fig. 6(c). It is clear that there are a number of ultrafine-equiaxed grains [see Fig. 6(d)] and nanotwins that coexist in the core. In Fig. 6(c), the nanotwins are indicated by the red circles. Image analysis revealed that the ultrafineequiaxed grains have a diameter of about 150 nm, while the nanotwins have dimensions of about 15 nm × 85 nm. Low density dislocations can be observed in the polygonal nanotwins, which is similar to the nanotwins produced through large plastic deformation in the literatures [54,55]. It is indicated that the nanotwins in the shear band should be deformation twins. In addition, the high-resolution TEM image of the ultrafine grains shows that the local grain-boundary segments tilt about 30°, as presented in Fig. 6(d). The rotation of grain-boundaries leading to the nanotwins which is similar to the rotation of grain boundaries leading to equiaxed grains proposed by Meyers et al. [64] indicates that the Rotational

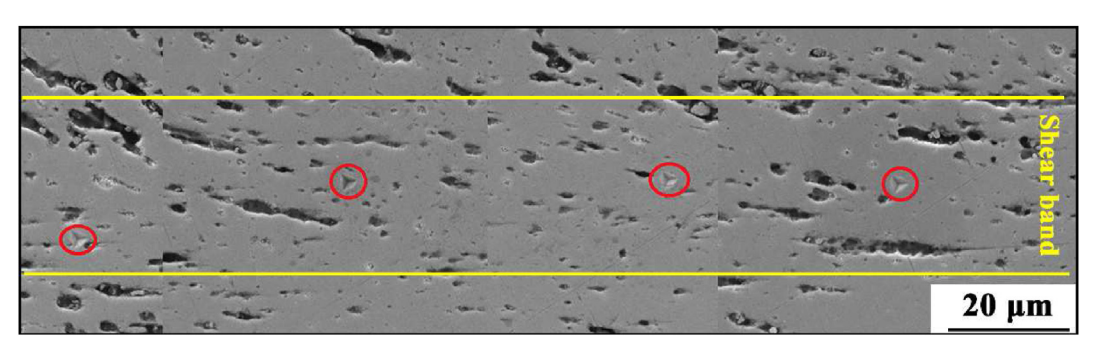


Fig. 8 – SEM of the indentation of a shear band in the PM CoCrFeMnNi HEA.

Dynamic Recrystallization (RDR) may occur in the shear band because the formation of nanograins needs the rotation of the elongated subgrains' boundaries, further discussed later [64].

The TEM image of nanotwins in the shear band is exhibited in Fig. 7. According to the image of the nanotwins [see Fig. 7(b)], the two sets of diffraction patterns correspond to the standard twinning structure, both of which are the single FCC structure. The twin plane is measured to be  $(\overline{1}1\overline{1})$ , and further analysis determined that the twin angle was about 70°.

Fig. 8 displays the SEM for the nanoindentation (labelled by a red circle) at the maximum load of 20 mN. It can be seen that the indents consist of a regular triangular pyramidal geometry. The applied load versus displacement and the creep displacement versus holding time for the shear band and the matrix in the PM CoCrFeMnNi HEA at the same strain rate are presented in Fig. 9(a)—(b), respectively. According to the figures, there are three stages during the nanoindentation tests,

namely the loading stage, holding stage, and unloading stage. The results from Fig. 9(a) indicate that the applied load in the ultrafine grains is larger than that in the matrix grains under the same displacement during the loading stage. It can also be noted that during the holding stage in the graph from Fig. 9(b), the values of the creep displacement for the shear band is about 20 nm, which is less than that of the matrix (about 26 nm). However, the creep rates are almost equal in both the shear band and matrix.

Fig. 10(a)-(b) present the applied load versus displacement and the creep displacement versus holding time for the shearband loading at strain rates ranging from 0.05 to  $0.5~\rm s^{-1}$ . It was found that during the loading stage, an increase in the strain rate leads to an increase in the applied load at the same displacement, which suggests that the strength of the shear band has a positive correlation with the strain rate. The strainrate dependence is also present in the nanoindentation creep-

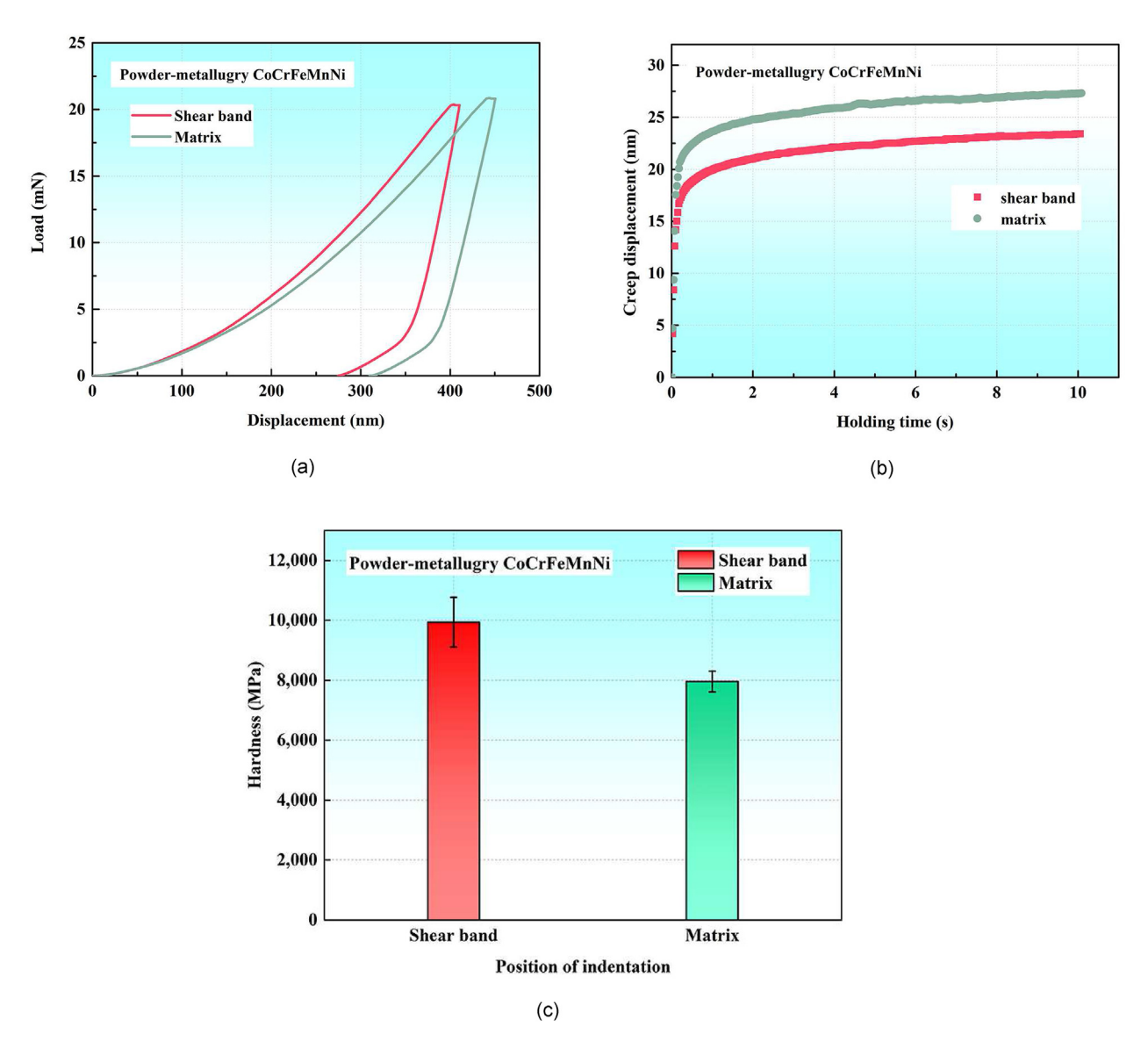
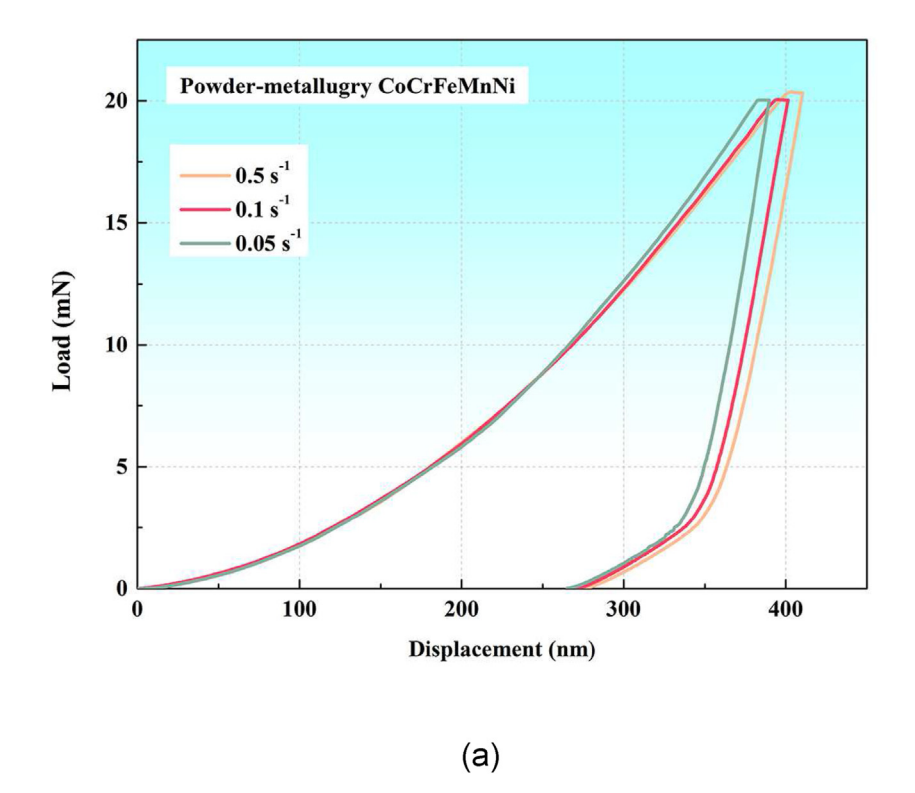


Fig. 9 – Nanoindentation of a shear band and matrix in the PM CoCrFeMnNi HEA loading at a strain rate of 0.5 s<sup>-1</sup>. (a) Load-displacement curves. (b) Creep-displacement curves. (c) Hardness comparison between shear band and matrix.

behavior of the alloy, i.e., the creep displacement and the creep rate increase with an increasing strain rate. From the nanoindentation-testing results (see Figs. 9 and 10), we can calculate the strengths of the nanotwins and the fine grains,

which were determined to be about 9940 MPa and 7959 MPa, respectively. Duan et al. [65] also found that the highest hardness of the nanograined body-centered cubic Mo alloys with grain sizes 11–13 nm is achieved about 17.3 GPa. A comparison



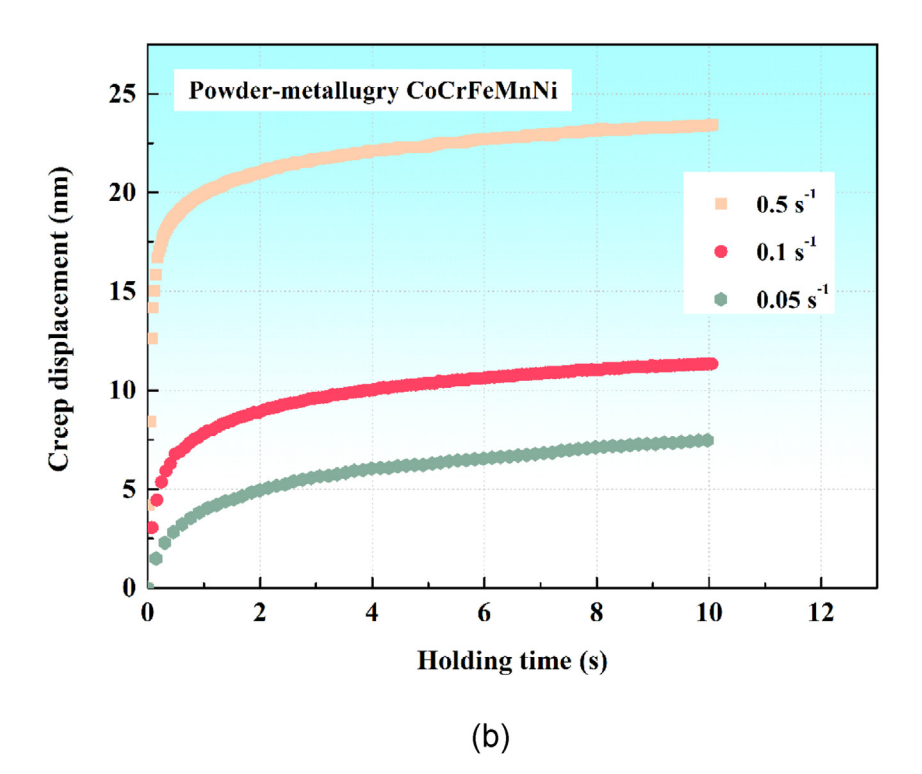


Fig. 10 – Nanoindentation of a shear band in the CoCrFeMnNi HEA loading at the strain rates of 0.05, 0.1, and 0.5 s<sup>-1</sup>. (a) Load-displacement curve. (b) Creep-displacement curves.

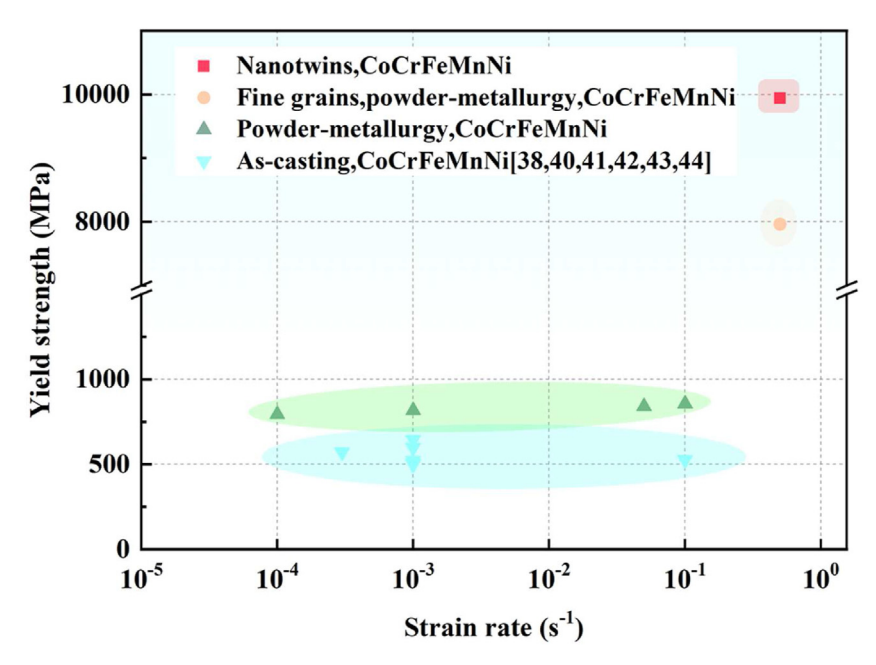


Fig. 11 — Comparison of the yield strength between the nanotwin and fine-grain specimens, the powder-metallurgy specimens, and the as-casting specimens [38,40—44].

of the strengths among the nanotwins and fine-grain specimens, the powder-metallurgy specimen, and the as-cast specimen [39,41–45] is shown in Fig. 11. The strength of the CoCrFeMnNi HEA prepared by the powder-metallurgy with nanotwins and fine grains are higher than that of the as-cast CoCrFeMnNi HEA. Thus, the introduction of nanotwins can further enhance the strength of the CoCrFeMnNi HEA.

## 4. Discussions

## 4.1. Serration behavior of the PM CoCrFeMnNi HEA

The CoCrFeMnNi HEA prepared by the powder metallurgy exhibited serrations when deformed at high strain rates (>1000 s<sup>-1</sup>). However, no serrations were observed in the PM CoCrFeMnNi HEA under quasi-static deformation (from 10<sup>-4</sup>  $s^{-1}$  to  $10^{-1}$   $s^{-1}$ ) according to our previous work [12]. Fig. 12 displays the results of the RCMSE analysis for the cylindrical samples deformed at strain rates of 1200  $s^{-1}$  - 2800  $s^{-1}$ . For these conditions, the sample entropy increased with increasing the scale factor, in general. This increase in the sample entropy means that for the cylindrical samples, the underlying dynamics of the serrated flow contain meaningful structural richness on all scales [23]. This richness may arise from a relatively-large number of interactions between defects (such as nanotwins) in the material during the serrated flow [25]. In contrast to the above behavior, the hat-shaped specimen exhibited a serrated flow in which the complexity of the fluctuations decreased with increasing the scale factor. This finding suggests that perhaps during the serrated flow, the stress-drop events consist of microstructural interactions that are spatially uncorrelated.

Furthermore, the sample-entropy curves (except for 2800 s<sup>-1</sup>) increased with increasing the strain rate, as exhibited in Fig. 12. This increasing trend has also been seen in the literature [56]. The increase in the complexity of the serrated flow with an increasing strain rate may be due to the overlapping of the deformation bands, which lead to rich scaling dynamics. As the strain rate is increased, new bands are formed in the field of the unrelaxed internal stresses, which results in the overlap of plastic events [56]. This overlapping behavior yields a serrated flow that consists of locking events that occur over a range of length scales, indicative of complex dynamics. Finally, the reason for the decrease in the complexity as the strain rate increased from  $2710 \text{ s}^{-1}$  to  $2800 \text{ s}^{-1}$ s<sup>-1</sup> is not entirely understood. Perhaps the decrease is due to compressing the material past a threshold strain rate such that the microstructural dynamics become less correlated at higher scales.

Fig. 13 shows the CCDF curves for the samples that underwent compression tests for the strain-rates ranging from about  $1200~\rm s^{-1}$  to about  $2800~\rm s^{-1}$ . It was found that the curves shifted to the right with increasing the strain rate. This result indicates that as the strain rate increases, the stress-drop magnitude increases. Here, the increased deformation rate is accompanied by a rise in the local-stress concentration, resulting in a greater obstruction of the dislocations and corresponding increase in the serration magnitude [22]. As can be observed in the inset, scaling collapse was achieved where the exponents,  $\kappa$  and  $\lambda$  [see Eq (C-2) from Appendix C], were found to be 1.30 and 1.01, respectively. Importantly, the above value for  $\kappa$  is in relatively-good agreement with the value of 1.5 proposed from MFT [26].

Therefore, the PM CoCrFeMnNi HEA exhibits mild serration behavior during high strain-rate deformation, which becomes more pronounced with an increasing strain rate, and the causes of this behavior can be explained by the RCMSE analysis and MFT theory. On the other hand, compared with the as-casting and forging CoCrFeMnNi HEA, the PM CoCrFeMnNi

HEA shows slighter serration behavior. It is indicated that the PM CoCrFeMnNi HEA exhibits the excellent deformation stability under high-speed deformation.

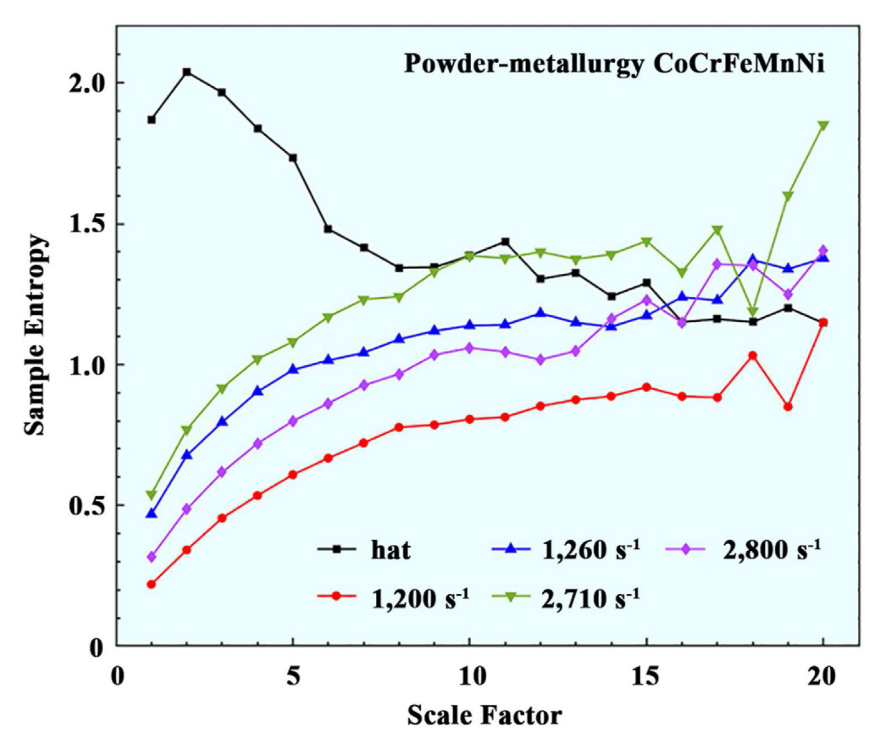


Fig. 12 – Sample-entropy results for the cylindrical and hat-shaped CoCrFeMnNi HEA samples tested at the strain rates ranging from about 1200  $\rm s^{-1}$  to about 2800  $\rm s^{-1}$ .

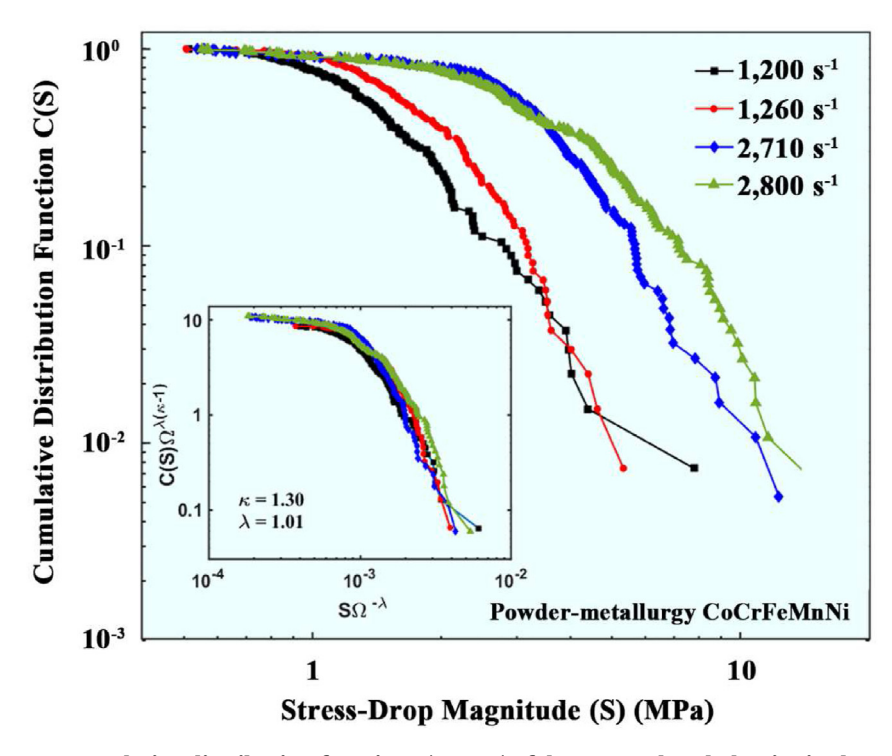


Fig. 13 — Complementary cumulative distribution functions (CCDFs) of the stress-drop behavior in the PM CoCrFeMnNi HEA. The scaling collapse is quantitatively verified for the exponent values of  $\kappa = 1.30$  and  $\lambda = 1.01$ .

# 4.2. Formation mechanism of nanotwins in the shear band

It is meaningful and valuable to study the strengthening and toughening of nanotwins for metal materials [57–62]. In this

study, nanotwins, formed instantaneously in the shear band, can significantly enhance the mechanical properties of the PM CoCrFeMnNi HEA. Severe plastic deformation will induce formation of the twins, and the RDR will induce the formation of the ultrafine grains. It is believed that a synergism of severe

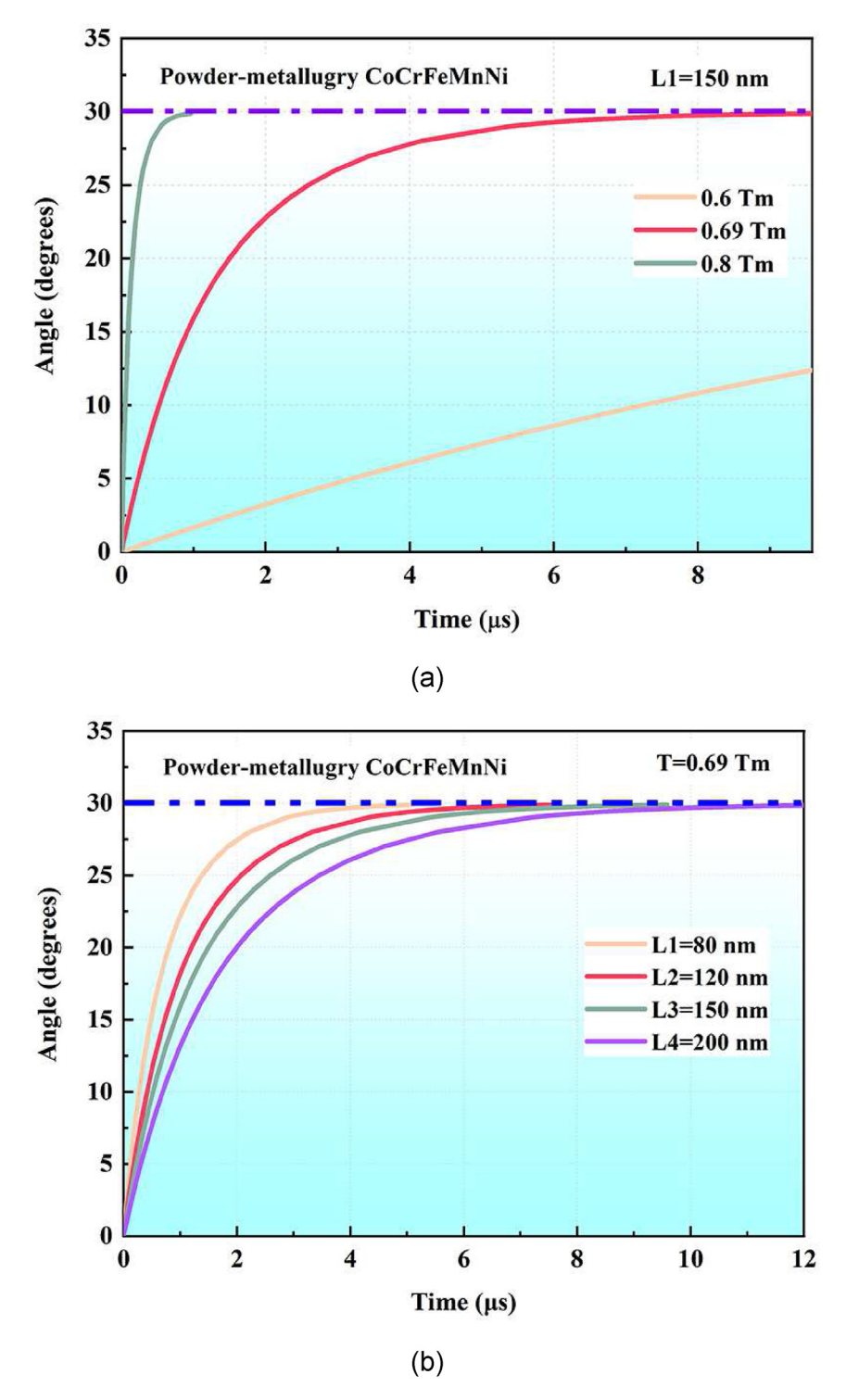


Fig. 14 – Kinetic curves of recrystallized grains generated by the subgrain-boundary rotation of the PM CoCrFeMnNi HEA. (a) Angle of rotation of the subgrain boundary in the CoCrFeMnNi HEA as a function of the needed time for different temperatures with  $L_1=150$  nm. (b) Angle of rotation of the subgrain boundary in the CoCrFeMnNi HEA as a function of the needed time for different subgrain sizes at  $0.69T_{\rm m}$ .

plastic deformation and RDR will induce the formation of the nanotwins.

On the one hand, sever plastic deformation will induce formation of the twins. There are two basic modes of plastic deformation at room temperature, slip and twinning. Twinning is the main deformation mode under high strain rate deformation because the value of the critical shear stress of twinning is insensitive to the strain rate. Twinning will occur when the value of the stress reaches the value of the critical shear stress during the deformation. The value of the critical shear stress of twinning  $\tau_p$  can be calculated, using Eq. (3) [66]:

$$\tau_p = \frac{2\alpha G b_p}{l} + \frac{\gamma}{b_p} \tag{3}$$

where  $\alpha$  reflects the characteristics of dislocations, G and  $b_p$  are the shear modulus and the modulus of the Burgers vector, respectively;  $\gamma$  and l are the stacking fault energy and grain size, respectively. For the CoCrFeMnNi HEA,  $\alpha$  is 1 [66], G is 80 GPa [67],  $b_p$  is 0.271 nm calculated from lattice constant,  $\gamma$  is 19 mJ/m² [68], and l is 3  $\mu$ m. The value of the critical shear stress of twinning of the PM CoCrFeMnNi HEA is about 85 MPa. While the maximum value of the shear stress reaches 635 MPa during the shear deformation (from Fig. 5(b)), which is much larger than the value of the critical shear stress. It is indicated that twins will be formed during the severe shear deformation.

On the other hand, the ultrafine grains in the shear band are formed instantaneously during the shear deformation, which exhibits the characteristics of grains formed by RDR. The kinetic verification of RDR in this work is calculated as follows. At high strain rates (>1000 s<sup>-1</sup>), the temperature rise in an adiabatic shear band can be calculated, using Eq. (4) [33]:

$$T = T_0 + \Delta T = T_0 + \eta / \rho C_v \cdot \int_{\varepsilon_s}^{\varepsilon_e} \sigma d\varepsilon$$
 (4)

where T and  $\Delta T$  are the temperature and temperature rise in the shear band, respectively;  $T_0$  and  $\rho$  are the initial deformation temperature and the mass density, respectively;  $C_v$  and  $\eta$  are the heat capacity and the fraction of the plastic energy converted to heat, respectively. Commonly  $\eta = 0.9$  [32]. For this alloy,  $\rho$  is 8.042 g/cm<sup>3</sup>,  $C_v$  is 430 J/kg, and  $T_0$  is 293 K. The melting point  $(T_m)$  of the PM CoCrFeMnNi HEA is about 1600 K.

The deformation-energy for the shear-localization process can be calculated from the shear-stress vs. shear-strain curve [Fig. 2(b)]. The details of the calculation process are explained in our previous work [63]. When the maximum shear strain reaches about 50, the temperature rise in the shear band is about 1110 K (T/ $T_m = 0.69$ ). Therefore, the temperature rise in the shear band is high enough to induce recrystallization for the CoCrFeMnNi HEA (0.4–0.5  $T_m$ ).

According to the theory of RDR mechanisms [64], the time needed for the fractured subgrain boundary to rotate about 30° can be calculated. In the present work, we can obtain the kinetic curves, as depicted in Fig. 14. Full details of the calculations are given in Appendix D.

In the HEA, the temperature increases from 0.6  $T_m$  to 0.8  $T_m$ at the subgrain size of about 150 nm [Fig. 14 (a)]. The subgrain size,  $L_1$ , increases from about 80 nm to

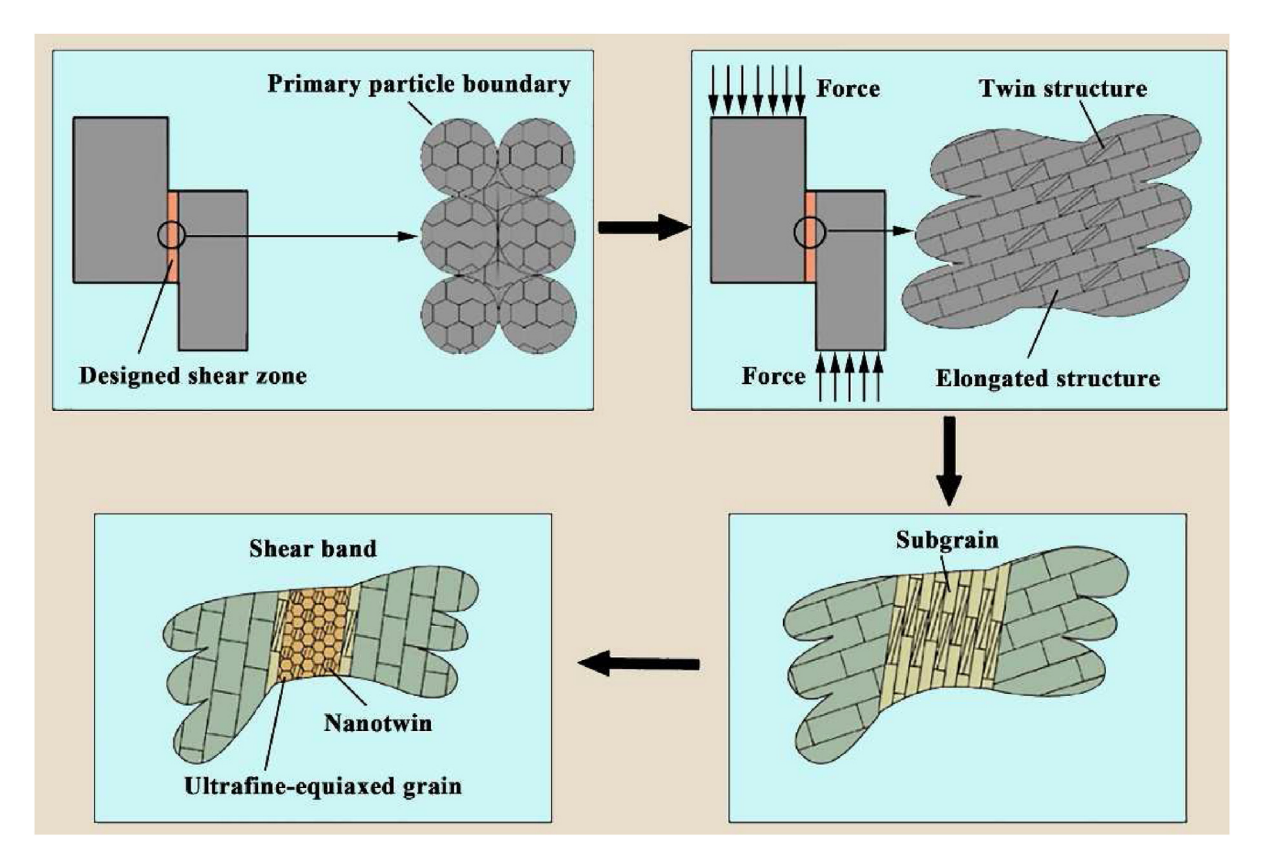


Fig. 15 - Schematic diagram of the microstructural evolution within a shear band in the CoCrFeMnNi HEA.

approximately 200 nm at the average elevated temperature of  $T=0.69~T_m$  (about 1100 K) [Fig. 14 (b)]. The rotation of a grain boundary is completed within about 10  $\mu$ m at the subgrain size of about 150 nm and temperature of ~1100 K. Moreover, the time needed for recrystallization will decrease with a smaller subgrain size and higher temperature [64]. Therefore, the deformation time (~135  $\mu$ s) is sufficient to form ultrafine-equiaxed grains by the subgrain-boundary rotation. Therefore, the RDR mechanism can result in ultrafine grains and nanotwins in the shear band of the PM CoCrFeMnNi HEA investigated in the current work.

The microstructural formation of nanotwins in the CoCr-FeMnNi HEA during shear deformation can be described as follows (Fig. 15). Firstly, twin structures form due to the severe plastic deformation. When the volume fraction of the twin reaches a critical value, further twinning becomes difficult to accommodate the subsequent strain. At that moment, both the grains with and without twins structures elongate into cell structures along the shear direction as the deformation continues. Secondly, the elongated cell structures split into several subgrains that are located by dense dislocation walls due to the strong shear deformation. Subsequently, the subgrains transform into approximately equiaxed micrograins due to the minimization of the interfacial energy. Finally, the sub-boundaries evolve into highly-misorientated grain boundaries. This phenomenon may occur by way of the local grain-boundary segments of the micrograins rotating about 30° to form high-angle grain boundaries. Hence, nanotwins are formed in the PM CoCrFeMnNi HEA by RDR.

## 5. Conclusions

The CoCrFeMnNi HEA prepared by powder metallurgy exhibits potential applications in the field for high-speed impact deformation due to its slight serration behavior and low adiabatic shear sensitivity. The results indicated that the mechanical properties of the HEA are significantly affected by the applied strain rate. Furthermore, the PM CoCrFeMnNi HEA exhibited serrations when the alloy was deformed at high strain rates. The results of the MFT analysis indicated that the magnitude of the serrations increased with the strain rate. This increase in the serration magnitude was attributed to an increase in the local-stress concentration that inhibit dislocation motion, resulting in more pronounced serrations. The results of the RCMSE analysis suggested that the cylindrical samples displayed serrations that were characterized by the dynamically-complex behavior. Also, the dynamical complexity of the serrations generally increased with the strain rate. The shear band with a width of about 20 microns was generated in the PM CoCrFeMnNi HEA when the value of the nominal strain reaches about 8.71.

Nanotwins, formed instantaneously in the shear band, can significantly enhance the mechanical properties of the PM CoCrFeMnNi HEA. The shear band in the PM CoCrFeMnNi HEA was distinguishable from the matrix by the boundary of the shear band. The region inside the boundary of a shear band consisted of twin and cell structures that had average dimensions of  $\sim 0.1$  microns  $\times 0.7$  microns and were highly elongated along the shear direction. The findings also revealed

that nanotwins and ultrafine-equiaxed grains with a diameter of about 150 nm were generated in the core of the shear band. The strength of the shear band with nanotwins and ultrafine-equiaxed grains was higher than that of the matrix grains. Moreover, nanotwins with the single FCC structure in the shear band have the twin plane of  $(\overline{1}1\overline{1})$  that can be formed via the RDR mechanism.

## **Author contribution**

Conceptualization, B. W. and P. L.; methodology, W. L., X. H., J. B., and B. W.; validation, B. W. and P. L.; formal analysis, B. W., W. L., J. B., and P. L.; investigation, B. W., W. L., X. H., and J. B.; resources, B. L.; data curation, B. W., W. L., X. H., J. B., and P. L.; writing-original draft preparation, B. W., P. L., B. L., W. L., X. H., and J. B.; writing-review and editing, B. W., W. L., J. B., and P. L.; visualization, W. L., X. H., and J. B.; supervision, B. W., B. L. and P. L.; project administration, B. W. and B. L.; funding acquisition, B. W. and B. L. and P.L..

## **Declaration of Competing Interest**

The authors declare that they have no known competing financial interests or personal relationships that could have appeared to influence the work reported in this paper.

## **Acknowledgments**

The present work was financially supported by the National Natural Science of China (Nos. 51771231 and 52020105013), and by the State Key Laboratory of Powder Metallurgy (No. 62102172). Peter K. Liaw thanks the support from (1) the National Science Foundation (DMR-1611180 and 1809640) and (2) the Army Research Office (W911NF-13-1-0438 and W911NF-19-2-0049). The authors wish to express their most sincere gratitudes to Professor Marc A. Meyers at the University of California, San Diego and Professor Yong Liu at the Central South University for their advice and helps. The authors would like to present their sincere thanks to Professors Xiang Zan, Yang Wang, and Yu Wang at the University of Science and Technology of China, and Mr. Ao Fu and Ms. Chu Wang at the Central South University, for the experimental works. The authors also would like to express their sincere thanks to Dr. Yinghong Lin at FEI Co. for the preparation of TEM samples.

## Appendix A. Supplementary data

Supplementary data to this article can be found online at https://doi.org/10.1016/j.jmrt.2022.09.106.

REFERENCES

 Miracle DB, Senkov ON. A critical review of high entropy alloys and related concepts. Acta Mater 2017;122:448-511.

- [2] Shi PJ, Li RG, Li Y, Wen YB, Zhong YB, Ren WL, et al. Hierarchical crack buffering triples ductility in eutectic herringbone high-entropy alloys. Science 2021;373(6557):912–8.
- [3] George EP, Curtin WA, Tasan CC. High entropy alloys: a focused review of mechanical properties and deformation mechanisms. Acta Mater 2020;188:435–74.
- [4] Jiang W, Yuan SY, Cao Y, Zhang Y, Zhao YH. Mechanical properties and deformation mechanisms of a Ni<sub>2</sub>Co<sub>1</sub>FeV<sub>0.5</sub>Mo<sub>0.2</sub> medium-entropy alloy at elevated temperature. Acta Mater 2021;213:116982.
- [5] Li WD, Xie D, Li DY, Zhang Y, Gao YF, Liaw PK. Mechanical behavior of high-entropy alloys. Prog Mater Sci 2021;118:100777.
- [6] Pan QS, Zhang LX, Feng R, Lu QH, An K, Chuang AC, et al. Gradient cell-structured high-entropy alloy with exceptional strength and ductility. Science 2021;374(6570):984–9.
- [7] Xu XD, Liu P, Tang Z, Hirata A, Song SX, Nieh TG, et al. Transmission electron microscopy characterization of dislocation structure in a face-centered cubic high-entropy alloy Al<sub>0.1</sub>CoCrFeNi. Acta Mater 2018;144:107–15.
- [8] Zhang Y, Zuo TT, Tang Z, Gao MC, Dahmen KA, Liaw PK, et al. Microstructures and properties of high-entropy alloys. Prog Mater Sci 2014;61:1—93.
- [9] Waseem OA, Ryu HJ. Powder metallurgy processing of a W<sub>x</sub>TaTiVCr high-entropy alloy and its derivative alloys for fusion material applications. Sci Rep 2017;7:1926.
- [10] Liu Y, Wang JS, Fang QH, Liu B, Wu Y, Chen SQ. Preparation of superfine-grained high entropy alloy by spark plasma sintering gas atomized powder. Intermetallics 2016;68:16–22.
- [11] Zhang AJ, Han JS, Meng JH, Su B, Li PD. Rapid preparation of AlCoCrFeNi high entropy alloy by spark plasma sintering from elemental powder mixture. Mater Lett 2016;181:82-5.
- [12] Wang BF, Huang XX, Fu A, Liu Y, Liu B. Serration behavior and microstructure of high entropy alloy CoCrFeMnNi prepared by powder metallurgy. Mater Sci Eng, A 2018;726:37–44.
- [13] Li ZZ, Zhao ST, Ritchie RO, Meyers MA. Mechanical properties of high-entropy alloys with emphasis on facecentered cubic alloys. Prog Mater Sci 2019;102:296–345.
- [14] Hayat MD, Singh H, He Z, Cao P. Titanium metal matrix composites: an overview. Compos Appl Sci Manuf 2019;121:418–38.
- [15] Zhang TW, Ma SG, Zhao D, Wu YC, Zhang Y, Wang ZH, et al. Simultaneous enhancement of strength and ductility in a NiCoCrFe high-entropy alloy upon dynamic tension: micromechanism and constitutive modeling. Int J Plast 2020;124:226–46.
- [16] Laktionova MA, Tabchnikova ED, Tang Z, Liaw PK. Mechanical properties of the high-entropy alloy Ag<sub>0.5</sub>CoCrCuFeNi at temperatures of 4.2-300K. Low Temp Phys 2013;39(7):630–2.
- [17] Choudhary BK. Influence of strain rate and temperature on serrated flow in 9Cr-1Mo ferritic steel. Mater Sci Eng, A 2013;564:303—9.
- [18] Zhang Y, Liu JP, Chen SY, Xie X, Liaw PK, Dahmen KA, et al. Serration and noise behaviors in materials. Prog Mater Sci 2017:90:358–460.
- [19] Oh S-K, Kilic ME, Seol J-B, Hong J-S, Soon A, Lee Y-K. The mechanism of dynamic strain aging for type A serrations in tensile flow curves of Fe-18Mn-0.55C (wt.%) twinninginduced plasticity steel. Acta Mater 2020;188:366-75.
- [20] Tirunlia AS, Hanemann T, Weiss K-P, Freudenberger J, Heilmaier M, Kauffmann A. Dislocation-based serrated plastic flow of high entropy alloys at cryogenic temperatures. Acta Mater 2020;200:980—91.
- [21] Wang BF, Yao XR, Wang C, Zhang XY, Huang XX. Mechanical properties and microstructure of a NiCrFeCoMn high-

- entropy alloy deformed at high strain rates. Entropy 2018;20(11):892.
- [22] Liu RY, Yao XR, Wang BF. Mechanical properties and serration behavior of a NiCrFeCoMn high-entropy alloy at high strain rates. Mater 2020;13(17):3722.
- [23] Costa M, Goldberger AL, Peng CK. Multiscale entropy analysis of complex physiologic time series. Phys Rev Lett 2002;89(6):068102.
- [24] Dahmen KA, Ben-Zion Y, Uhl JT. Micromechanical model for deformation in solids with universal predictions for stressstrain curves and slip avalanches. Phys Rev Lett 2009;102(17):175501.
- [25] Zhang BB, Liaw PK, Brechtl J, Ren JL, Guo XX, Zhang Y. Effects of Cu and Zn on microstructures and mechanical behavior of the medium-entropy aluminum alloy. J Alloys Compd 2020;820:153092.
- [26] Antonaglia J, Xie X, Schwarz G, Wraith M, Qiao JW, Zhang Y. Tuned critical avalanche scaling in bulk metallic glasses. Sci Rep 2014;4:4382.
- [27] Li Z, Zhao S, Diao H, Liaw PK, Meyers MA. High-velocity deformation of Al<sub>0.3</sub>CoCrFeNi high-entropy alloy: remarkable resistance to shear failure. Sci Rep 2017;7:42742.
- [28] Meyers MA, Li ZZ, Zhao ST, Wang BF, Liu Y, Liaw PK. Shear localization of fcc high-entropy alloys. In: Proceeding of 12<sup>th</sup> international conference on the mechanical and physical behavior of materials under dynamic loading. vol. 183. Arcachon, France; 2018. p. 03028.
- [29] Yang ZL, Yang MX, Ma Y, Zhou LL, Cheng WQ, Yuan FP, et al. Strain rate dependent shear localization and deformation mechanisms in the CrMnFeCoNi high-entropy alloy with various microstructures. Mater Sci Eng, A 2020;798:139854.
- [30] Li ZZ, Zhao ST, Alotabi SM, Liu B, Wang BF, Meyers MA. Adiabatic shear localization in the CrMnFeCoNi high-entropy alloy. Acta Mater 2018;151:424—31.
- [31] Wang BF, Huang XX, Liu Y, Liu B. Mechanical properties and shear localization of high entropy alloy CoCrFeMnNi prepared by powder metallurgy. In: TMS 2018 147<sup>th</sup> annual meeting and exhibition supplemental proceedings, the minerals, metals and materials series. Cham: Springer; 2018. p. 469–80.
- [32] Dodd B, Bai YL. Adiabatic shear localization: frontiers and advances. 2nd. ed. London: Elsevier Science Ltd; 2012.
- [33] Omar MF, Akil HM, Ahmad ZA, Mazuki AAM, Yokoyama T. Dynamic properties of pultruded natural fibre reinforced composites using Split Hopkinson Pressure Bar technique. Mater Des 2010;31(9):4209–18.
- [34] Li Q, Xu YB, Lai ZH, Shen LT, Bai YL. Dynamic recrystallization induced by plastic deformation at high strain rate in a Monel alloy. Mater Sci Eng, A 2000;276(1–2):250–6.
- [35] Yu TX, Qiu XM. Introduction to impact dynamics. Singapore: John Wiley & Sons; 2018. Singapore Pte. Ltd.
- [36] Qiu CL, Panwisawas C, Ward M, Basoalto HC, Brooks JB, Attallah MM. On the role of melt flow into the surface structure and porosity development during selective laser melting. Acta Mater 2015;96:72—9.
- [37] Chen Z, Wang BF, Duan BH, Zhang XY. Mechanical properties and microstructure of laser welded FeCoNiCrMn highentropy alloy. Mater Lett 2020;262:127060.
- [38] Wu S-D, Wu C-W, Lin S-G, Lee K-Y, Peng C-K. Analysis of complex time series using refined composite multiscale entropy. Phys Lett 2014;378(20):1369-74.
- [39] Fu JX, Cao CM, Tong W, Hao YX, Peng LM. The tensile properties and serrated flow behavior of a thermomechanically treated CoCrFeNiMn high-entropy alloy. Mater Sci Eng, A 2017;690:418–26.
- [40] Carroll R, Lee C, Tsai C-W, Yeh J-W, Antonaglia J, Brinkman BAW, et al. Experiments and model for serration

- statistics in low-entropy, medium-entropy, and high-entropy alloys. Sci Rep 2015;5:16997.
- [41] Gali A, George EP. Tensile properties of high- and medium-entropy alloys. Intermetallics 2013;39:74—8.
- [42] Shahmir H, Mousavi T, He JY, Lu ZP, Kawasaki M, Langdon TG. Microstructure and properties of a CoCrFeNiMn high-entropy alloy processed by equal-channel angular pressing. Mater Sci Eng, A 2017;705:411–9.
- [43] Laplanche G, Kostka A, Horst OM, Eggeler G, George EP. Microstructure evolution and critical stress for twinning in the CrMnFeCoNi high-entropy alloy. Acta Mater 2016;118:152–63.
- [44] Laplanche G, Kostka A, Reinhart C, Hunfeld J, Eggeler G, George EP. Reasons for the superior mechanical properties of medium-entropy CrCoNi compared to high-entropy CrMnFeCoNi. Acta Mater 2017;128:292–303.
- [45] Wu Z, Parish CM, Bei H. Nano-twin mediated plasticity in carbon-containing FeNiCoCrMn high entropy alloys. J Alloys Compd 2015;647:815—22.
- [46] Chen AY, Ruan HH, Wang J, Chan HL, Wang Q, Li Q, et al. The influence of strain rate on the microstructure transition of 304 stainless steel. Acta Mater 2011;59(9):3697–709.
- [47] Li W, Li S, Liu J, Zhang A, Zhou Y, Wei QS, et al. Effect of heat treatment on AlSi<sub>10</sub>Mg alloy fabricated by selective laser melting: microstructure evolution, mechanical properties and fracture mechanism. Mater Sci Eng, A 2016;663:116–25.
- [48] Li XP, Wang XJ, Saunders M, Suvorova A, Zhang LC, Liu YJ, et al. A selective laser melting and solution heat treatment refined Al-12Si alloy with a controllable ultrafine eutectic microstructure and 25% tensile ductility. Acta Mater 2015;95:74—82.
- [49] Zheng LW, Nie HH, Zhang WG, Liang W, Wang YD. Microstructural refinement and improvement of mechanical properties of hot-rolled Mg-3Al-Zn alloy sheets subjected to pre-extrusion and Al-Si alloying. Mater Sci Eng, A 2018;722:58–68.
- [50] Karaköse E, Keskin M. Microstructure evolution and mechanical properties of intermetallic Ni-xSi (x=5,10,15,20) alloys. J Alloys Compd 2012;528:63-9.
- [51] Afkhami S, Dabiri M, Heidi P, Björk T. Effects of manufacturing parameters and mechanical post-processing on stainless steel 316L processed by laser powder bed fusion. Mater Sci Eng, A 2021;802:140660.
- [52] Meng LF, Zhang Z, Zhang YL, Zhang JX, Yang X, Gao HL, et al. The influence of stacking fault energy on mechanical properties of Cu-Al-Zn alloys processed by surface mechanical attrition treatment. Mater Sci Eng, A 2019;744:235–40.
- [53] Kumar N, Ying Q, Nie X, Mishra RS, Tang Z, Liaw PK, et al. High strain-rate compressive deformation behavior of the

- $Al_{0.1}$ CrFeCoNi high entropy alloy. Mater Des 2015;86:598–602.
- [54] Li XY, Sun SJ, Zou Y, Zhu Q, Tian YZ, Wang JW. Twin-coupled shear bands in an ultrafine-grained CoCrFeMnNi highentropy alloy deformed at 77K. Mater Res Lett 2022;10(6):385–91.
- [55] Zhang Z, Jiang ZH, Xie YH, Chan SLL, Liang JM, Wang J. Multiple deformation mechanisms induced by pre-twinning in CoCrFeNi high entropy alloy. Scripta Mater 2022;207:114266.
- [56] Sarkar A, Barat P, Mukherjee P. Multiscale entropy analysis of the Portevin-Le Chatelier effect in an Al-2.5%Mg alloy. Fractals 2010;18(3):319—25.
- [57] Wang JJ, Tao NR, Lu K. Revealing the deformation mechanisms of nanograins in gradient nanostructured Cu and CuAl alloys under tension. Acta Mater 2019;180:231–42.
- [58] Li XY, Jin ZH, Zhou X, Lu K. Constrained minimal-interface structures in polycrystalline copper with extremely fine grains. Science 2020;370(6518):831–6.
- [59] Jin ZH, Li XY, Lu K. Formation of stable Schwarz crystals in polycrystalline copper at the grain size limit. Phys Rev Lett 2021;127:136101.
- [60] Cheng Z, Zhou HF, Lu QH, Gao HJ, Lu L. Extra strengthening and work hardening in gradient nanotwinned metals. Science 2018;362(6414):559–63.
- [61] Pan QS, Zhou HF, Lu QH, Gao HJ, Lu L. History-independent cyclic response of nanotwinned metals. Nature 2017;551(7679):214-7.
- [62] Lu QH, You ZS, Huang XX, Hansen N, Lu L. Dependence of dislocation structure on orientation and slip systems in highly oriented nanotwinned Cu. Acta Mater 2017;127:85–97.
- [63] Wang BF, Liu ZL, Wang B, Zhao ST, Sun JY. Microstructural evolution in adiabatic shear band in the ultrafine-grained austenitic stainless steel processed by multi-axial compression. Mater Sci Eng, A 2014;611:100–7.
- [64] Meyers MA, Xu YB, Xue Q, Perez-Prado MT, McNelley TR. Microstructural evolution in adiabatic shear localization in stainless steel. Acta Mater 2003;51(5):1307–25.
- [65] Duan FH, Naunheim Y, Schuh CA, Li Y. Breakdown of the Hall-Petch relationship in extremely fine nanograined bodycentered cubic Mo alloys. Acta Mater 2021;213:116950.
- [66] Wan HY, Luo XM, Li X, Liu W, Zhang GP. Nanotwinsenhanced fatigue resistance of ultrathin Ag films for flexible electronics applications. Mater Sci Eng, A 2016;676:421–6.
- [67] Huang H, Li XQ, Dong ZH, Li W, Huang S, Meng DQ, et al. Critical stress for twinning nucleation in CrCoNi- based medium and high entropy alloys. Acta Mater 2018;149:388–96.
- [68] Zaddach AJ, Niu C, Koch CC, Irving DL. Mechanical properties and stacking fault energies of NiFeCrCoMn high-entropy alloy. J Occup Med 2013;65(12):1780–9.